NÖHÜ Müh. Bilim. Derg. / NOHU J. Eng. Sci., 2025; 14(4), 1339-1351
Niğde Ömer Halisdemir Üniversitesi Mühendislik Bilimleri Dergisi
Niğde Ömer Halisdemir University Journal of Engineering Sciences
Araştırma makalesi / Research article
www.dergipark.org.tr/tr/pub/ngumuh / www.dergipark.org.tr/en/pub/ngumuh

Ergimiş tuz aşındırmasıyla sentezlenen Klor-Termine MXenelerde elektrolit-bağımlı lityum interkalasyonu

Electrolyte-dependent lithium intercalation in Chlorine-Terminated MXenes synthesized via molten salt etching

Esra Kılavuz[1,*]

[1] *Niğde Ömer Halisdemir University, Central Research Laboratory, 51240, Niğde, Türkiye*

Abstract

MXenes are two-dimensional materials with a wide range of applications. The electrochemical properties of these materials are largely determined by their surface terminations (functional groups). Traditionally, hydrofluoric acid (HF) is used for MXene synthesis, which typically results in -O, -F, and -OH surface terminations. However, these groups can limit the MXene's conductivity, stability, electrochemical behavior, and chemical reactivity. In this study, we synthesized multilayer $Ti_3C_2Cl_2$ MXenes via a molten salt etching route using $ZnCl_2$, a method that enables the controlled introduction of chlorine surface terminations instead of conventional HF-based approaches. We systematically investigated the lithium-ion intercalation behavior of these chlorine-terminated MXenes (MS-$Ti_3C_2Cl_2$) in organic electrolytes—DMSO, PC, and ACN—employing a three-electrode Swagelok cell configuration. Electrochemical analysis showed that electrolyte composition strongly affects Li^+ intercalation behavior. PC enabled pseudocapacitive storage via full desolvation, while DMSO offered high Coulombic efficiency (~100%) with mixed kinetics. ACN caused solvated Li^+ co-intercalation and poor performance. b-value analysis indicated diffusion-controlled behavior in DMSO (b = 0.663) versus capacitive dominance in ACN (b = 0.884). These results highlight the critical role of termination chemistry and solvent choice in optimizing MXene electrodes for advanced energy storage with customized interfacial properties.

Keywords: MXene, Organic electrolyte, Li-intercalation, LIBs, Molten salt etching

Öz

MXeneler, geniş uygulama alanlarına sahip iki boyutlu malzemelerdir. Bu malzemelerin elektrokimyasal özellikleri, yüzeylerindeki sonlanma grupları (fonksiyonel gruplar) tarafından büyük ölçüde belirlenir. Geleneksel olarak, MXene sentezinde hidroflorik asit (HF) kullanılır ve bu yöntemle yüzeyde genellikle-O, -F ve -OH gibi sonlanma grupları oluşur. Ancak bu gruplar, MXene'nin iletkenliğini, kararlılığını, elektrokimyasal davranışını ve kimyasal reaktivitesini sınırlayabilir. Bu çalışmada, geleneksel HF-aşındırma metodu yerine kontrollü klor terminasyonu sağlayan $ZnCl_2$ kullanılarak ergimiş tuz aşındırma yöntemiyle çok katmanlı $Ti_3C_2Cl_2$ MXeneler sentezlenmiştir. Klor-terminasyonlu bu MXenelerin (MS-$Ti_3C_2Cl_2$) lityum-iyon interkalasyon davranışı, DMSO, PC ve ACN organik elektrolitlerinde üç elektrotlu Swagelok hücre düzeneği kullanılarak sistematik olarak incelenmiştir. Elektrokimyasal ölçümler, elektrolit bileşiminin interkalasyon dinamiği üzerinde belirleyici bir etkiye sahip olduğunu ortaya koymuştur. PC elektroliti, tam desolvasyon yoluyla psödokapasitif Li^+ depolanmasını sağlarken, DMSO yüksek Coulomb verimliliği (~%100) ve karmaşık yük depolama kinetiği sergilemiştir. Buna karşılık, ACN'de solvatlı Li^+ iyonlarının ko-interkalasyonu performans düşüşüne yol açmıştır. Kinetik analiz, b-değeri kantifikasyonu kullanılarak gerçekleştirilmiş ve DMSO için difüzyon-kontrollü davranış (b = 0,663), ACN için ise yüzey-dominant kapasitif davranış (b=0,884) gözlemlenmiştir. Bu bulgular, yüksek performanslı enerji depolama uygulamaları için MXene-tabanlı elektrotların optimizasyonunda terminasyon kimyası ve çözgen seçiminin önemini vurgulamaktadır.

Anahtar kelimeler: MXene, Organik elektrolit, Li interkalasyon, LİB, Ergimiş tuz aşındırma

1 Introduction

The increasing demand for high-performance electrochemical energy storage systems has intensified the search for advanced charge-carrying materials capable of meeting the energy and power density requirements of modern technologies [1–4]. However, a significant limitation remains: their typically slow charging rates, which are largely due to diffusion-limited redox reactions [1,5]. To overcome this challenge and simultaneously achieve high power and high energy density, substantial research has focused on developing high-performance electrode materials. These materials facilitate fast and reversible redox reactions, allowing them to circumvent the diffusion constraints of conventional batteries and outperform the limited capacity of electric double-layer capacitors.

* Sorumlu yazar / Corresponding author, e-posta / e-mail: kesra@ohu.edu.tr (E. Kılavuz)
Geliş / Received: 26.06.2025 Kabul / Accepted: 12.08.2025 Yayımlanma / Published: 15.10.2025
doi: 10.28948/ngumuh.1727823

Among emerging candidates, two-dimensional (2D) materials have attracted widespread attention [6–8]. As with graphene, large-area, high-quality 2D crystals are crucial for exploring new physical phenomena and realizing practical applications, especially in electronics and optoelectronics [9,10]. Transition metal carbides represent a large class of materials that combine the beneficial characteristics of ceramics and metals, owing to the incorporation of carbon atoms into metal lattices. Within this family, MXenes have emerged as particularly promising due to their unique structural, electronic, optical, hydrophilic, plasmonic, and chemical properties [7,11–14]. These features make MXenes highly suitable for a broad range of applications, including electrochemical energy storage, electromagnetic shielding, catalysis, chemical sensing, photoelectric conversion, and wearable electronics [7,15–17].

Discovered in 2011, MXenes are typically synthesized by selectively etching the A-element from layered MAX phases, resulting in structures composed of transition metal carbides, nitrides, or carbonitrides [18]. Their large surface area, high electrical conductivity, and tunable surface chemistry make them ideal for use in lithium-ion batteries, supercapacitors, and sodium-ion batteries [19–22]. MXenes can be produced using either top-down or bottom-up synthesis methods, each with its own advantages and drawbacks [23,24]. The top-down approach, currently the most widely adopted, involves selectively etching the A layers using strong acids such as hydrofluoric acid or fluoride-containing acidic solutions. This is followed by intercalation and delamination to obtain few-layer or monolayer flakes. While effective and scalable, this method introduces surface terminations—typically oxygen, hydroxyl, and fluorine groups—which significantly alter MXenes' electronic structure, charge transport behavior, and chemical reactivity [6,20,23,25]. These surface terminations are difficult to avoid and remain a major challenge for fully realizing the potential of pristine MXenes [5,7,26].

Moreover, MXenes produced via chemical etching often have limited lateral sizes, typically ranging from a few hundred nanometres to around 10 µm [27]. They also tend to exhibit structural defects and irregularities [28]. As with other 2D materials like graphene, the lack of large-area, high-quality MXene crystals restricts the ability to investigate their intrinsic properties. To address these issues, increasing attention has turned to bottom-up synthesis techniques such as chemical vapor deposition (CVD), which offer greater control over crystal structure, composition, and surface chemistry [21,27,29]. Although still in early stages, CVD-based methods have shown promise in producing MXene-like structures with improved properties [27,30–33]. For instance, vapor-phase synthesis techniques have yielded TiC films with enhanced conductivity and fewer surface terminations. Other approaches, such as liquid metal-based synthesis, provide a promising route for producing termination-free 2D carbides and nitrides [34,35].

Some modifications to the traditional etching process, such as using LiF/HCl instead of hydrofluoric acid, have improved the safety profile of synthesis [11,32,33,36]. However, these methods still do not eliminate the use of fluorine, and surface functional groups introduced during etching continue to affect MXenes' electronic band structures [34,37–39]. This limits their tunability and hinders applications such as photocatalysis, where surface chemistry plays a critical role.

Controlling surface terminations is one of the most important factors in tuning MXene properties yet remains among the least explored experimentally. The type and proportion of surface terminations are typically dictated by the etching agent, with oxygen and fluorine dominating and hydroxyl groups playing a lesser role. Notably, recent studies have demonstrated the synthesis of MXenes with alternative terminations, such as chlorine, bromine, and iodine, by employing molten salts or Lewis acidic melts [24,40,41]. These terminations have shown improved stability and open new pathways for property tuning [42]. Given the strong influence of surface terminations on MXenes' performance and the emerging ability to control them more precisely, there is a growing need for a comprehensive understanding of how different chemical species interact with various MXene structures [10,17,26,28,43]. Chen et all. reported the exclusive method for preparing MXenes in the air using low-melting-point eutectic chlorides as a reaction salt bed and Lewis-acid salts as etchants [44].

In our study, we adopted a modified top-down approach using molten salt etching to synthesize MXenes while minimizing the introduction of surface terminations. Unlike conventional acid-based methods, molten salt etching offers a cleaner route for removing the A-layer from the MAX phase, helping preserve a more pristine MXene surface. The resulting material was integrated into working electrodes using a polyvinylidene fluoride (PVDF) binder, and its electrochemical performance was evaluated in the context of lithium-ion intercalation. What distinguishes this study is the electrochemical evaluation of MS-$Ti_3C_2Cl_2$ in its non-delaminated form, with a particular focus on elucidating the lithium-ion intercalation behavior under such structural constraints.

This approach allows for a clearer assessment of the intrinsic properties of MXenes, decoupled from the effects of surface terminations. While previous studies have shown that surface terminations significantly impact electrochemical behavior, the underlying mechanisms remain unclear [23,42,44]. In this study, we aim to elucidate the lithium intercalation mechanism in non-delaminated molten salt–synthesized MXenes, thereby contributing to a deeper understanding of their role as charge-storage materials.

2 Material and method

The MAX phase was purchased Shandong Mengnan New Materials Technology Co. Ltd. From China. Anhydrous $ZnCl_2$ (Sigma-Aldrich, >99%).

2.1 Synthesis of MS-MXene with various surface terminations

MXenes with tailored surface terminations were synthesized via a direct redox reaction between the A-site element of the MAX phase and the cation of a selected Lewis acidic molten salt, as previously reported [32,35,45–48]. In

our procedure, Ti_3AlC_2 was etched using a molten salt mixture composed of $ZnCl_2$ in a KCl:LiCl eutectic (1:1 molar ratio), where Zn^{2+} ions served as the oxidizing agent to selectively remove Al from the MAX structure. This redox reaction is driven by the difference in standard electrode potentials between Zn^{2+}/Zn (−0.76 V vs Cl_2/Cl^-) and Al^{3+}/Al (−1.85 V vs Cl_2/Cl^-), leading to the formation of a $Ti_3C_2T_x/Zn$ intermediate product, as represented in Equation (1). To eliminate residual Zn^{2+} impurities introduced during synthesis, a magnetic separation technique was employed, yielding high-purity Cl-terminated $Ti_3C_2T_x$ MXenes (designated as Cl–Ti_3C_2) in Equation (2). Compared to conventional HF-etched MXenes terminated with F and O groups—characterized by strong Ti–F (569 ± 33 kJ/mol) and Ti–O (672 ± 9 kJ/mol) bonds—the Ti–Cl bonds in Cl–Ti_3C_2 MXenes exhibit significantly lower bond dissociation energy (405 ± 11 kJ/mol). This suggests more labile surface chemistry, which may enhance ion transport kinetics. Nevertheless, a persistent limitation of the molten salt route remains the difficulty in effectively delaminating the resulting MXene structures into few-layer or monolayer forms.

$$Ti_3AlC_{2(s)} + 3ZnCl_{2(l)} \rightarrow Ti_3C_{2(s)} + 2AlCl_{3(g)} + 3Zn_{(s)} \quad (1)$$

$$Ti_3C_{2(s)} + 2ZnCl_{2(l)} \rightarrow Ti_3C_2Cl_{2(s)} + 2Zn_{(s)} \quad (2)$$

To synthesize $Ti_3C_2Cl_2$ MXene, anhydrous $ZnCl_2$ (Sigma-Aldrich, >99%) was employed as the Lewis acid. Due to its hygroscopic nature, all handling steps were conducted in an argon-filled glovebox to prevent moisture exposure. Initially, $ZnCl_2$ was ground in a ball mill device for 7 minutes until it formed a fine powder. Subsequently, 5 grams of Ti_3AlC_2 MAX phase and 50 grams of powdered $ZnCl_2$ were placed in a 250 mL glass beaker and mixed using a homogenizer at 100 rpm for 3 minutes. The resulting powder mixture was transferred to an alumina crucible, sealed in a ziplock bag under argon to maintain an inert atmosphere, and removed from the glovebox to avoid humidity contact.

The sealed crucible was then introduced into a tube furnace (MTI) under a continuous argon flow (99% purity, 5 SCCM) and heated to 640 °C at a rate of 5 °C/min. The reaction was maintained for 4 hours, followed by cooling at the same rate. After thermal treatment, the reaction product (molten salt-etched MXene, or MS-MXene) was retrieved and washed to remove unreacted $ZnCl_2$ and metallic Zn byproducts. This was done by immersing the product in 150 mL of 12 M HCl in a 500 mL glass sealed beaker and stirring at 300 rpm for 5 hours at room temperature.

The acidified MXene was then divided between three 50 mL centrifuge tubes, rinsed three times with deionized (DI) water via centrifugation at 1400 rcf for 5 minutes each. This washing step was critical for removing fine MXene flakes that could otherwise obstruct the pores of the filtration membrane and hinder the filtration process. The sediment containing multilayer MXene was then redispersed in DI water and filtered using a 5 µm polycarbonate membrane. To ensure complete removal of residual ions and small particles, approximately 2 liters of DI water were used during the filtration process. Following filtration, the wet MXene powder was air-dried for 1 hour and then further dried under vacuum oven at 45 °C overnight.

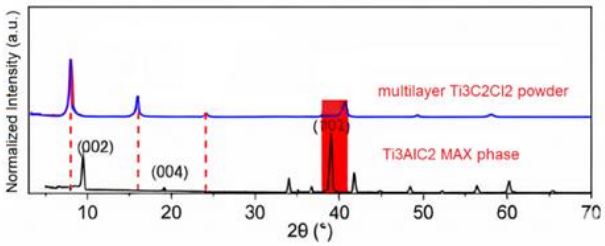

Figure 1. Characterization of halogenated Ti_3C_2 MXenes. XRD patterns show the (0002), (0004), and (0006) peaks of the multilayer MS-$Ti_3C_2Cl_2$ and $Ti_3Al_2C_2$ obtained in the present work

Figure 1. shows the X-ray diffraction (XRD) patterns of the MAX phase precursor (black plot), the MXene after removal from the molten salt bath (blue plot). The selective etching process causes a significant weakening of the characteristic (104) peak of Ti_3AlC_2 at 39° (as shown in the red area of Figure 1) and results in a shift of the (002) peak from 9.9° to a lower 2θ angle of 9.6°, indicating the successful transformation of Ti_3AlC_2 into layered $Ti_3C_2T_x$ (MXene). Meanwhile, the (002) peak became exceptionally intense and sharp, suggesting an increase in the d-spacing (defined as the sum of the interlayer distance and the thickness of the 2D sheet) of the MS-Ti_3C_2Cl2, indicating thicker and more well-defined layers.

Electrochemical studies were conducted on MS-$Ti_3C_2Cl_2$ in its undelaminated state. The structural and compositional characteristics of this material have been further elucidated in a detailed study by Zhang et al., published in Chemistry of Materials. Their work provides complementary insights into the crystalline structure, surface terminations, and interlayer chemistry, supporting the interpretation of electrochemical performance presented here [48].

2.1.1 Electrode preparation

To investigate the distinct electrochemical behavior of chlorine-terminated MXenes compared to those with conventional surface terminations, we we conducted cyclic voltammetry (CV), electrochemical impedance spectroscopy (EIS), Charge /Discharge (GDC) electrochemical tests using a 7-µm-thick MXene film. This film thickness was specifically chosen to minimize ion transport limitations associated with electrode architecture [49–51]. All measurements were carried out using a Swagelok cell configured in a three-electrode system, employing a lithium metal wire as the reference electrode and a carbon film as the counter electrode. Unlike traditional setups utilizing glassy carbon, stainless steel was used as the current collector in this study.

To ensure consistency across all tests, MXene electrodes were fabricated under controlled conditions, maintaining uniform surface area, thickness, mass loading, and contact integrity with the current collector. This rigorous

standardization allowed any observed differences in electrochemical performance to be attributed exclusively to the nature of the electrolyte.

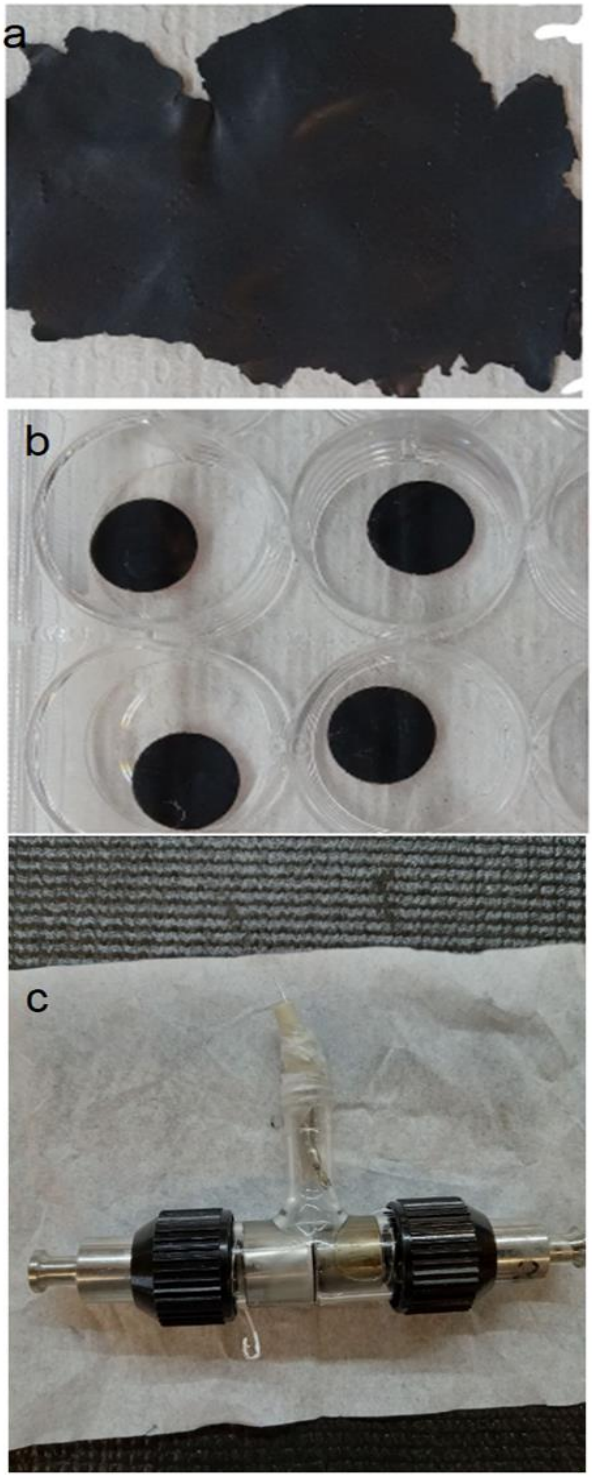

Figure 2. (a) MS-MXene electrode film, (b) 7 mm punched MS-MXene working electrode, (c) assembled Swagelok cell

For this purpose, organic electrolytes containing 1 M LiTFSI dissolved in dimethyl sulfoxide (DMSO), acetonitrile (ACN), and propylene carbonate (PC) were employed. These electrolytes were selected to promote effective lithium-ion intercalation into the hydrophobic layered structure of MS-$Ti_3C_2Cl_2$, enabling a comparative evaluation of electrolyte-dependent intercalation behavior. The working electrode was prepared via doctor blade coater on copper foil. A slurry was prepared by uniformly dispersing $Ti_3C_2Cl_2$ MXene with polyvinylidene fluoride (PVDF) binder in N-methyl-2-pyrrolidone (NMP) to ensure homogeneous thickness and even distribution in the resulting film (Figure 2a).

The resulting slurry was cast onto a flat substrate and dried under vacuum under vacuum at 40° C, 24 hours. Discs with a diameter of 7 mm were subsequently punched out and used as the working electrode (Figure 2b) Sealed electrochemical cells were assembled in an argon-filled glovebox (O_2 and H_2O < 0.1 ppm). Laboratory-assembled compression cells with a Swagelok®-style design (Figure 2c) were used for electrochemical testing. The cell configuration included: working electrode is $Ti_3C_2Cl_2$ film (7 mm diameter), counter electrode: carbon film (12 mm diameter) reference electrode: Lithium metal (Li) Separator: Two stacked discs of celgard membrane (14 mm diameter) and electrolyte: 1 M lithium bis (trifluoromethanesulfonyl) imide (LiTFSI) dissolved in a ternary solvent mixture of ACN, DMSO, and PC in equal volume ratios (Figure 2c).The schematic configuration of the assembled Swagelok cell and the electrode film are shown in Figure 2c.

2.1.2 Electrochemical characterizations

A series of electrochemical characterizations were conducted to assess the electrochemical performance of multilayer film MS-$Ti_3C_2Cl_2$. Figures 3a to 3c present the CV profiles of both MS-$Ti_3C_2Cl_2$ recorded at a scan rate of 1 mV s^{-1} with varying negative cut-off potentials. The measurements were performed in three different organic electrolytes: 1 M LiTFSI dissolved in DMSO (Figure 3a), PC (Figure 3b), and ACN (Figure 3c), allowing for a comparative analysis of their electrochemical behavior under different electrolyte environments.

To improve the energy density of supercapacitors (SCs), nonaqueous electrolytes are commonly employed due to their ability to extend the operating potential window. Since energy density scales with the square of the cell voltage, significant research has focused on developing electrolytes that are not only electrochemically stable but also highly conductive and capable of supporting wide voltage ranges [5,39,52,53]. By switching from aqueous to organic electrolytes, the operating voltage of electric double-layer capacitors (EDLCs) can be increased from approximately 1 V to between 2.5 and 2.7 V [31,54].

Organic electrolytes typically consist of conductive salt solutions, such as tetraethylammonium tetrafluoroborate ($TEABF_4$) or lithium hexafluorophosphate ($LiPF_6$), dissolved in organic solvents like ACN or PC. Among these, PC is often preferred due to its higher flash point and lower toxicity compared to ACN, offering improved safety and environmental compatibility without compromising performance.

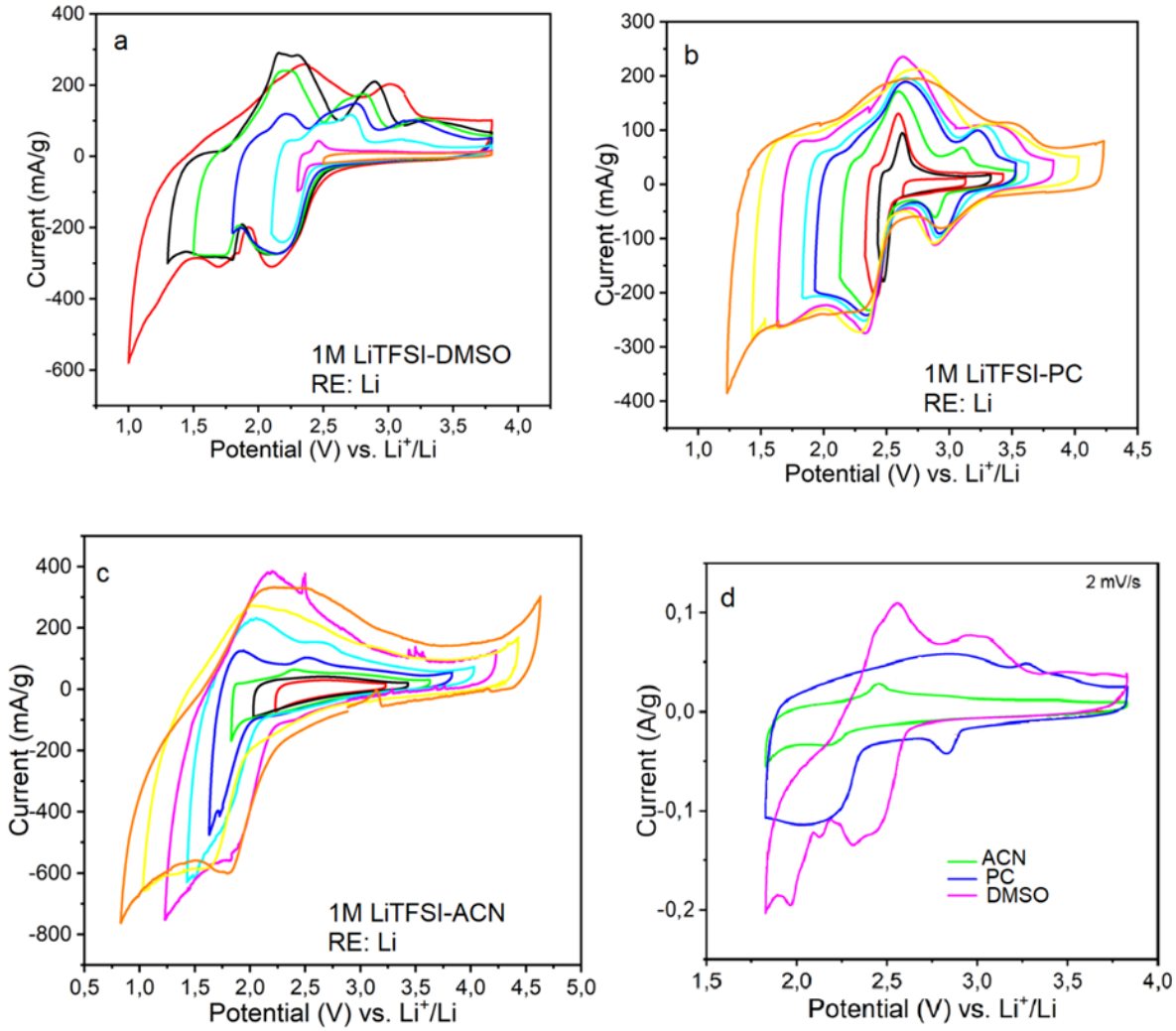

Figure 3. Cyclic voltammetry voltage window profiles for (a) MS- $Ti_3C_2Cl_2$ for 1M LiTFSI DMSO electrolyte, (b) MS- $Ti_3C_2Cl_2$ for 1M LiTFSI PC electrolyte, (c) MS- $Ti_3C_2Cl_2$ for 1M LiTFSI ACN, (d) comparision of MS- $Ti_3C_2Cl_2$ in three different electrolytes

This study explores the pseudocapacitive charge storage behavior of MS-$Ti_3C_2Cl_2$ by systematically assessing its rate capability, kinetic analysis of charge storage, and electrochemical voltage window. Furthermore, it highlights the effectiveness of electrode design strategies in enabling efficient energy storage and rapid power delivery, even under ultra-high-rate conditions.

The operational voltage limit of ACN-based electrolytes is primarily constrained by the electrochemical decomposition of acetonitrile, which initiates at potentials more negative than 1.2 V vs. Li. This limitation arises despite acetonitrile's well-documented advantage of high electronic conductivity, as illustrated in Figure 3c. In contrast, such degradation behavior was not observed in carbonate-based (PC) or DMSO-based electrolytes, making the observed instability in ACN an unexpected and noteworthy finding.

To evaluate electrochemical performance under these constraints, electric double-layer capacitors (EDLCs) were systematically assembled using MS-$Ti_3C_2Cl_2$ electrodes. Initial electrochemical testing was carried out with appropriate safety voltage cut-offs applied to both the electrodes and the complete device, ensuring operation within stable and secure potential ranges.

Figure 3d presents CVs recorded at a scan rate of 2 mV s^{-1} for MS-$Ti_3C_2Cl_2$ in 1 M LiTFSI dissolved in three different organic solvents: DMSO, ACN, and PC. The results reveal distinct variations in electrochemical behavior depending on the solvent environment. Surface terminations on MXene materials are known to play a critical role in dictating their charge storage characteristics; however, the precise mechanisms remain inadequately understood. Recent findings by Liu et al. [46] demonstrated that the introduction of oxygen-containing surface groups can activate pseudocapacitive redox processes in electrochemical activity through surface chemistry modulation [55-58].

Cl-terminated Ti_3C_2 MXenes under nonaqueous conditions, suggesting a potential route to enhance MXenes possess a partially delaminated layered structure, enabling

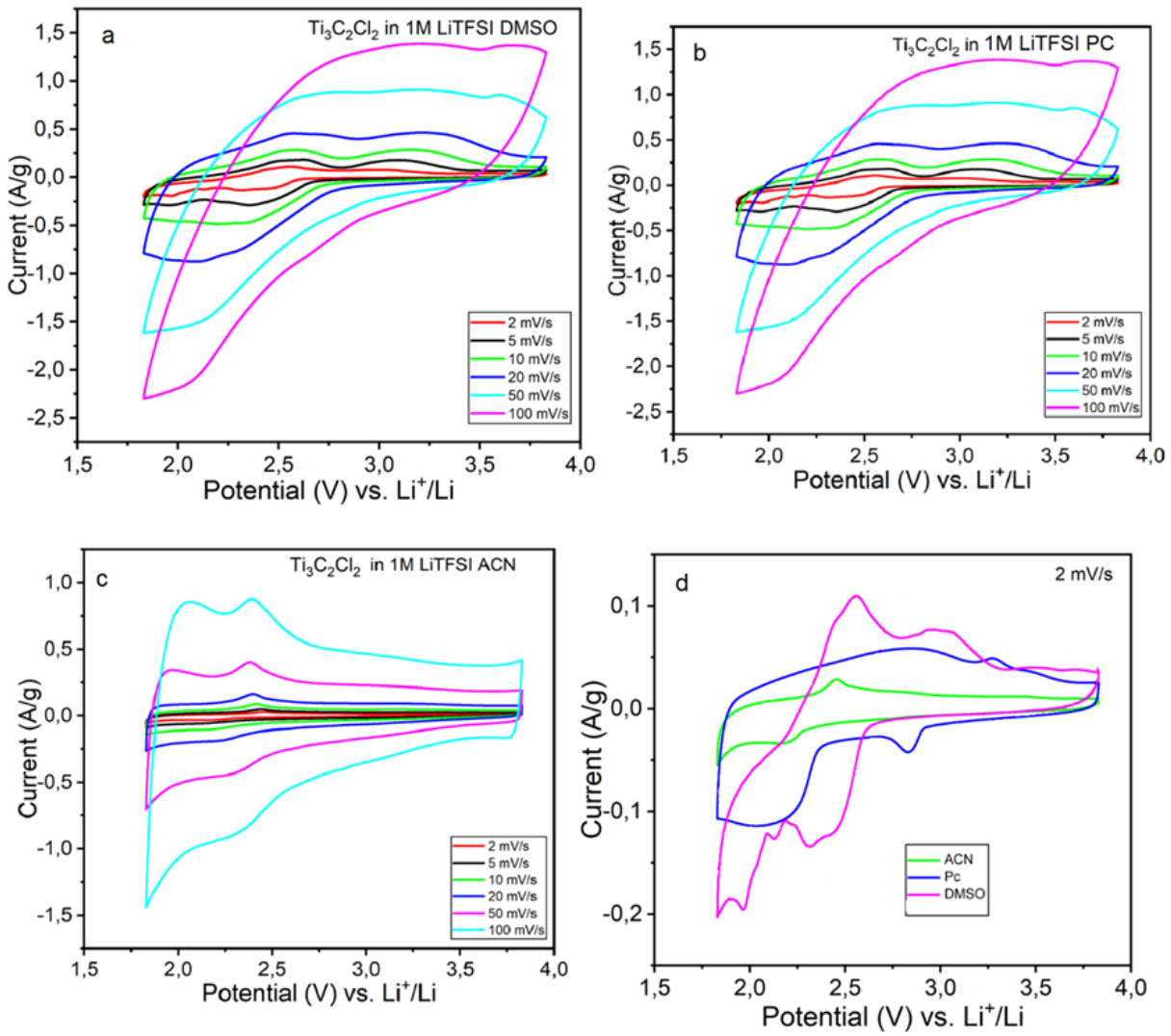

Figure 4. Cyclic voltammetry voltage window profiles for (a) MS- $Ti_3C_2Cl_2$ for 1M LiTFSI DMSO electrolyte, (b) MS-$Ti_3C_2Cl_2$ for 1M LiTFSI PC electrolyte, (c) MS- $Ti_3C_2Cl_2$ for 1M LiTFSI ACN, (d) comparision of MS- $Ti_3C_2Cl_2$ in three different electrolytes

both ion intercalation and electrical double-layer (EDL) formation to contribute to charge storage. As shown in Figure 4, the cyclic voltammograms of non-delaminated MS-MXene deviate from the ideal rectangular shape typical of EDL-dominated behavior, particularly in ACN electrolyte. Voltammograms of MS-$Ti_3C_2Cl_2$ in LiTFSI/organic solvent electrolytes exhibit distinct features, with two pairs of symmetric peaks during cycling, suggesting that the charging process is primarily governed by rapid redox reactions linked to intercalation in Figure 4a-c. Given the small ionic radius of Li^+ (0.9 Å) and the hydrophobic nature of the MS-$Ti_3C_2Cl_2$ electrode, which favors interactions with non-polar organic solvents, it can be inferred that Li^+ desolvation involves direct surface interactions with MS-$Ti_3C_2Cl_2$ [59–61]. The hydrophobic nature of MS-$Ti_3C_2Cl_2$ MXene, characterized by its non-polar basal planes, preferentially repels polar solvents. However, the presence of polar -Cl terminations introduces localized hydrophilic sites, enabling weak interactions with polar aprotic solvents. The extent of these interactions varies significantly depending on the solvent's polarity, donor number (DN), and molecular structure, which in turn influence Li^+ solvation and interfacial charge transfer.

In DMSO, a highly polar solvent (DN ≈ 29.8), Li^+ forms a stable solvation shell (e.g., $[Li(DMSO)_4]^+$), creating a high energy barrier for desolvation. While the hydrophobic MXene surface resists DMSO wetting, the -Cl terminations provide limited anchoring points for Li^+, leading to Faradaic redox peaks in CV rather than capacitive behavior.

PC, with moderate polarity (DN ≈ 15.1), solvates Li^+ less strongly than DMSO, resulting in a partially stable solvation shell (e.g., $[Li(PC)_4]^+$). The bulkier molecular structure of PC compared to DMSO restricts its access to MXene interlayers, leading to mixed capacitive and Faradaic behavior in CVs, where sluggish Li^+ desolvation and solvent co-intercalation contribute to broad redox humps.

ACN, a weakly coordinating solvent (DN ≈ 14.1), forms labile Li^+ solvation complexes (e.g., $[Li(ACN)_4]^+$) that readily dissociate at the MXene interface. The small molecular size of ACN facilitates rapid ion transport and enhances double-layer capacitance, yielding near-rectangular CVs with minimal Faradaic distortion. Despite the MXene's hydrophobicity, ACN's weak solvation enables efficient Li^+ adsorption at -Cl sites, promoting capacitive charge storage. Consequintly, when MS-MXene electrodes are employed in nonaqueous electrolytes, their CV profiles deviate from the conventional capacitive shape. For instance, the MS-$Ti_3C_2Cl_2$ electrode in a Li^+-containing DMSO electrolyte displays distinct redox activity, with a cathodic peak at 3.0 V and an anodic peak at 2.3 V (Figure 4a). Similarly, in ACN-based electrolyte, redox-like features appear at 2.25 V (anodic) and 2.4 V (cathodic) (Figure 4c), while the PC electrolyte exhibits peaks at 3.4 V (cathodic) and 2.7 V (anodic). These non-ideal CV profiles imply that charge storage in MS-MXenes involves Faradaic processes alongside capacitive mechanisms.

The electronic structure of MXene is significantly altered during charge/discharge cycles in aqueous electrolytes, where electron transfer into its unoccupied states drives its reduction. [21,56,62]. These conditions likely enhance electronic interactions, particularly through d-orbital overlap, between the intercalated species and MXene's transition metal layers. In contrast to aqueous systems, the lower solvation energy in nonaqueous electrolytes facilitates partial cation desolvation at the MXene interface [39,42,50,63], enabling orbital hybridization between intercalated cations and MXene's electronic structure. Furthermore, Li^+ intercalation/deintercalation in MS-$Ti_3C_2Cl_2$ MXene proceeds in a stepwise manner, as evidenced by multiple distinct redox peaks in the cyclic voltammetry profiles (Figure 4d). These peaks correspond to the sequential insertion/extraction of Li^+ ions within the MXene interlayer gaps, highlighting the multi-stage nature of the process.

This study highlights the critical influence of electrolyte solvent choice on lithium-ion intercalation behavior in MS-$Ti_3C_2Cl_2$ MXene electrodes. When using lithium bis(trifluoromethylsulfonyl)imide (LiTFSI) in propylene carbonate (PC), significant desolvation of Li^+ ions occurs within the $Ti_3C_2Cl_2$ interlayers, promoting a pseudocapacitive intercalation mechanism. In contrast, electrolytes containing ACN or DMSO exhibit significantly lower capacitance due to co-intercalation of solvated Li^+ species. This phenomenon contrasts with conventional expectations from carbon-based supercapacitors, where ACN typically delivers superior performance owing to its high ionic conductivity. These results demonstrate that optimal electrolyte selection must account for the unique interfacial properties of MXene electrodes to maximize charge storage efficiency and electrochemical performance.

Figure 5 presents the Coulombic efficiency (CE) of lithium-ion cells utilizing MS- $Ti_3C_2Cl_2$ in three different electrolytes, as DMSO black, PC red, and ACN green lines—as a function of cycle number. CE, defined as the ratio of discharge capacity to charge capacity within a given cycle, is a critical metric for assessing the reversibility and stability of electrochemical processes. In high-performance lithium-ion batteries, CE is typically expected to approach 100%, indicating minimal side reactions and efficient lithium cycling [56,56,64].

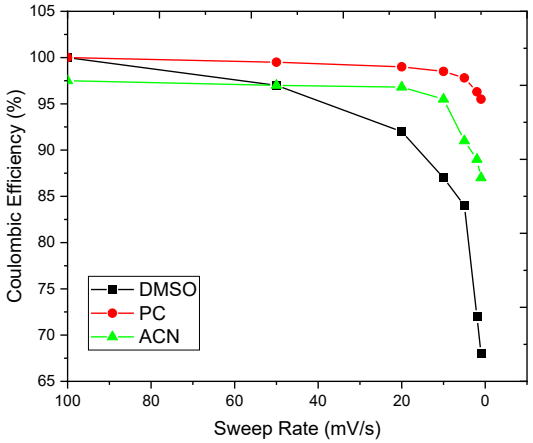

Figure 5. Coulombic of MS- $Ti_3C_2Cl_2$ in three different electrolytes

Among the tested electrolytes, the DMSO-based system exhibited the most stable behavior, maintaining a CE consistently near 100% throughout all cycles. This result indicates excellent electrochemical stability and negligible parasitic reactions, highlighting DMSO as a highly promising solvent for long-term cycling applications. The PC-based electrolyte also maintained a high CE, closely approaching 100% during the majority of the cycling period. However, a slight decline was observed after approximately 45 cycles, suggesting the onset of minor degradation or side reactions, although the overall performance remained robust.

In contrast, the ACN-based system demonstrated comparatively lower CE values across the cycling range. Notably, a significant drop in CE was observed after around 40 cycles, implying an increase in side reactions or lithium consumption. This trend indicates that ACN in particular undelaminated MS-MXene, may be less suitable for prolonged cycling, potentially due to reduced electrochemical stability or solvent decomposition under operational conditions.

2.1.3 Kinetic analysis of charge storage mechanisms in different electrolyte systems

To elucidate the charge storage behavior of the system, the relationship between peak current (i) and sweep rate (ν) was investigated using CV. This relationship follows a power law of the form in Equation (3):

$$i=av^b \tag{3}$$

where a is a constant and b is the kinetic parameter that indicates the dominant charge storage mechanism. A b-value of 0.5 corresponds to a diffusion-controlled (battery-type) process, while a b-value approaching 1 suggests a surface-controlled (capacitor-like) behavior [1,42,65].

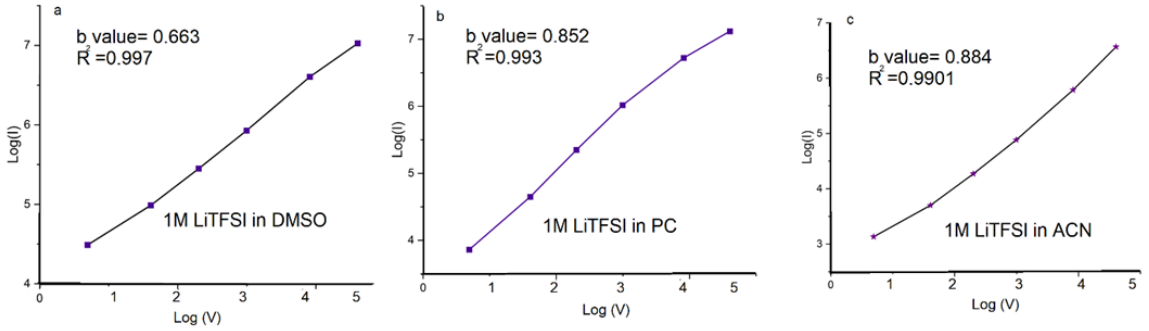

Figure 6. Determination of the b-value using the peak current relationship to sweep rate (1−100 mV s^{-1})

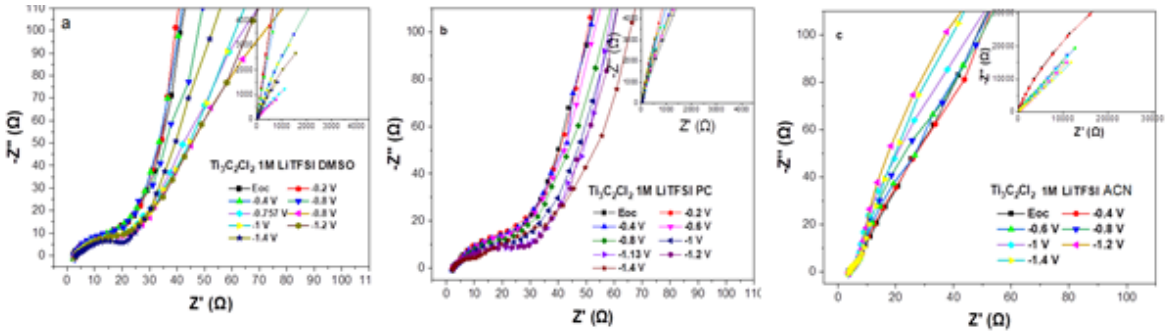

Figure 7. The electrochemical impedance spectroscopy plots recorded at various bias potentials. The Nyquist plots for MS- $Ti_3C_2Cl_2$ for (a) 1M LiTFSI DMSO (b) PC and (c) ACN electrolytes

Figure 6 shows the log(i) versus log(ν) plots for 1 M LiTFSI in three different solvents: DMSO, PC, and ACN. The slope of the fitted line in each case corresponds to the b-value, which provides insight into the kinetics of lithium-ion storage in each electrolyte environment. The b-value is calculated to be 0.663, indicating that the charge storage process in DMSO is governed by a mixed mechanism, with a dominant contribution from diffusion-controlled behavior.

This suggests the involvement of ion diffusion into bulk material or interlayer sites (Figure 6a). A higher b-value of 0.852 is observed for the PC-based system, implying a predominantly capacitive process with faster surface-controlled kinetics. This behavior indicates that Li^+ ions can be efficiently adsorbed at the electrode surface or readily intercalated into near-surface sites Figure 6b. The ACN system exhibits the highest b-value of 0.884, further approaching the ideal capacitive limit. This result points to a highly surface-dominated charge storage process, which may be attributed to the lower viscosity and faster ionic mobility in ACN compared to DMSO and PC Figure 6c.

The coefficient of determination (R^2) values for all three fits exceed 0.99, confirming the strong linearity and reliability of the kinetic model used. These results reveal a clear solvent-dependent trend in the charge storage kinetics, transitioning from diffusion-controlled (DMSO) to increasingly capacitive behavior (PC and ACN). Such variations in electrochemical behavior underscore the critical role of solvent properties in determining ion transport and charge storage mechanisms in Li-ion systems.

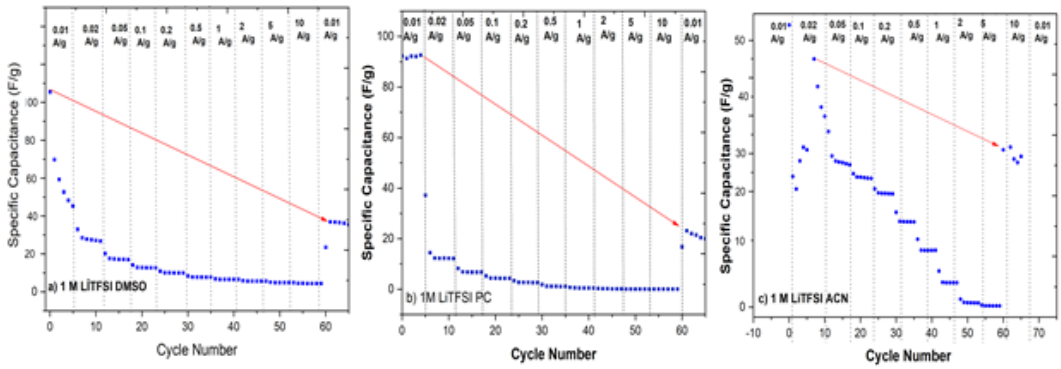

Figure 8. Galvanostatic charge/discharge curves at different current densities (a) MS- $Ti_3C_2Cl_2$ for 1M LiTFSI DMSO electrolyte, (b) MS- $Ti_3C_2Cl_2$ for 1M LiTFSI PC electrolyte, (c) MS- $Ti_3C_2Cl_2$ for 1M LiTFSI ACN

Electrochemical impedance spectroscopy (EIS) measurements were conducted for each of the three electrolytes at open circuit voltage (OCV) and at various bias potentials relative to Li to evaluate the electrochemical performance of the MS-$Ti_3C_2Cl_2$ MXene material (Figure 7. a-c). The Nyquist plots consistently exhibited a high-frequency semicircle followed by a rapid increase in the imaginary component of the impedance at low frequencies. The high- frequency semicircle corresponds to a charge-transfer resistance of approximately 20 Ω cm^2, which is nearly three times greater than that observed in a porous MXene electrode within a propylene carbonate-based electrolyte [26]. The equivalent series resistance, determined from the real-axis intercept of the Nyquist plots in Figure 7a-c, follows an increasing order for the solvents studied: DMSO and then PC, consistent with the trend of decreasing electrolyte conductivity [27,31]. At OCV, the MS-$Ti_3C_2Cl_2$ electrode exhibits typical capacitive behavior in both DMSO- and PC-based electrolytes, with a small high-frequency loop indicative of interfacial impedance at the electrode/current-collector interface, and a pronounced low-frequency rise. The inset of Figure 7c shows a mid-frequency region with a 90° slope, which indicates that both the PC and DMSO systems have similar ion diffusion limitations when they're at their resting potentials. However, when we look at the EIS plots at the anodic and cathodic peak potentials, we see that the systems don't behave like an ideal capacitor in the low-frequency range. Instead, both the imaginary and real parts of the impedance increase steadily.

This behavior suggests that the solvent in the DMSO system is helping to facilitate redox-like reactions and the transport of lithium ions within the MS-$Ti_3C_2Cl_2$ electrode. This is surprising because it's a different outcome than what's expected from water-based electrolytes, which typically have high ionic conductivity.

Additionally, when EIS spectra were taken at the maximum negative potential for each system (Figure 7a-c), all of the Nyquist plots showed a departure from ideal capacitive behavior at low frequencies. We also observed a slight increase in ion diffusion resistance, indicated by a 45° linear segment, compared to the open-circuit voltage (OCV) spectra. These results support the idea that the charge-storage mechanism of the MS-$Ti_3C_2Cl_2$ electrode isn't just based on capacitance.

The steep slope of the imaginary components at lower frequencies indicates that the kinetics of capacitive charge storage are more likely than those of a diffusion-controlled process. This inference is supported by the lack of a Warburg region, typically observed as a 45-degree line, in the mid-frequency range. Upon closer examination of the low-frequency domain, which is indicative of the charge storage mechanism, it is observed that the MS-MXene electrodes exhibit the most significant deviation from the ideal 90-degree phase angle. This deviation corroborates the CV signatures previously noted for these electrodes [66], Notably, a pronounced divergence is detected at the potentials corresponding to the onset of lithium intercalation within DMSO and PC electrolytic mediums (Figure 7c), which is attributable to CV voltammograms that are reminiscent of redox activity.

GCD measurements were performed to evaluate the specific capacitance behavior of the electrode material in three different electrolyte systems: 1 M LiTFSI in DMSO, PC, and ACN. While the DMSO-based electrolyte exhibited the highest initial specific capacitance (>100 F/g), a sharp and irreversible drop occurred immediately after the first few cycles (Figure 8). The PC-based system showed a similarly steep decrease, stabilizing at low capacitance values (~10 F/g), and the ACN-based system, although initially more gradual in its decline, ultimately reached near-zero performance (Figure 8b-c.). This pronounced degradation in all three systems originates from the structural limitations of the MXene electrode. The material, synthesized via molten salt etching with chlorine termination, was not delaminated, resulting in insufficient interlayer spacing. This narrow gallery structure critically hinders lithium-ion intercalation, especially under high-rate conditions. During the initial cycles, limited ion insertion can still occur, driven by surface-controlled kinetics; however, the lack of expanded interlayer pathways significantly restricts diffusion-controlled charge storage mechanisms. As a result, the electrode fails to sustain reversible lithium-ion transport, leading to rapid capacitance loss. These findings highlight the fundamental importance of structural engineering—particularly delamination—in enabling efficient ion accessibility and achieving stable electrochemical performance in MXene-based systems. Among the tested electrolytes, the highest specific capacitances were obtained as 5.47 F g^{-1} for ACN, 19.35 F g^{-1} for DMSO, and 16.22 F g^{-1} for PC, corresponding to approximately 3.04, 10.75, and 9.01 mAh g^{-1}, respectivel. In comparison to the present results the specific capacitances reported for $Ti_3C_2T_x$-based electrodes in the literature are substantially higher. For example, pristine $Ti_3C_2T_x$ in 1 M H_2SO_4 has demonstrated values up to 246 F g^{-1}[67], three-dimensional $Ti_3C_2T_x$@CNT hybrid aerogels have reached ≈468 F g^{-1} [68], and composite systems such as $Ti_3C_2T_x$/PANI/PVDF and $Ti_3C_2T_x$/NiO have delivered 895 and 892 F g^{-1} [69], respectively, compared to ≈359 F g^{-1} for pristine $Ti_3C_2T_x$ in the same study. The comparatively lower capacitance observed in this work can be attributed to the use of non-delaminated, chloride-terminated Ti_3C_2 prepared via molten salt etching. Such a structure inherently limits ion accessibility by restricting interlayer spacing and modifying surface chemistry, thereby impeding Li^+ insertion kinetics. The superior performance in aqueous media arises from their high ionic conductivity and small hydrated ion sizes, which facilitate rapid ion transport and efficient access to active sites. In contrast, organic electrolytes generally exhibit lower ionic conductivities and larger solvated Li^+ radii, factors that hinder intercalation kinetics. Moreover, the solvent dipole moment and its interaction with the MXene surface tension play a decisive role: high-dipole solvents can alter the surface energy of chloride-terminated Ti_3C_2, influencing the wetting behavior, double-layer formation, and desolvation energy barrier for Li^+. In the present study, the use of non-delaminated,

chloride-terminated Ti_3C_2 synthesized via molten salt etching further restricted the interlayer spacing, compounding the ion transport limitations inherent to organic systems. These results underscore the combined influence of electrolyte properties, surface terminations, and interlayer architecture in determining the electrochemical performance of MXenes.

3 Conclusion

This study elucidates the critical role of electrolyte solvent selection in modulating lithium-ion intercalation dynamics and charge storage behavior in chlorine-terminated MS-$Ti_3C_2Cl_2$ MXene electrodes. Comparative analysis of PC, DMSO, and ACN-based electrolytes revealed distinct electrochemical performance trends governed by solvent-specific interactions. PC electrolytes demonstrated superior pseudocapacitive intercalation characteristics, achieving complete Li^+ desolvation and stable charge storage, while DMSO exhibited exceptional electrochemical stability with near-ideal Coulombic efficiency (~100%) throughout cycling. In contrast, ACN electrolytes, despite their high ionic conductivity, suffered from significant capacity fade beyond 40 cycles due to unfavorable solvated Li^+ co-intercalation. Kinetic analysis through b-value quantification further highlighted this solvent dependence, showing a progressive transition from diffusion-controlled behavior (DMSO, b= 0.663) to surface-dominated capacitive processes (ACN, b = 0.884). The hydrophobic MS-$Ti_3C_2Cl_2$ surface preferentially facilitated direct Li^+ interactions in PC, whereas polar solvents like DMSO and ACN introduced competing solvation effects that altered charge storage pathways. Among the tested electrolytes, the highest specific capacitances were obtained as 5.47 F g^{-1} for ACN, 19.35 F g^{-1} for DMSO, and 16.22 F g^{-1} for PC, corresponding to approximately 3.04, 10.75, and 9.01 mAh g^{-1}, respectively, within a 2 V operating window. These findings establish clear structure-property-performance relationships between MXene termination chemistry and electrolyte components, providing a framework for rational electrolyte design. The demonstrated superiority of PC and DMSO systems, coupled with fundamental insights into interfacial charge transfer mechanisms, offers actionable guidance for developing optimized MXene-based energy storage devices. Future research directions should explore ternary solvent mixtures and surface termination engineering to further enhance MXene-electrolyte compatibility and device longevity, advancing the frontier of high-performance energy storage materials.

Conflict of interest

The author declares that there is no conflict of interest.

Similarity rate (iThenticate): 15%

References

[1] T. Hu, Y. Chen, H. Liu, L. Liu, C. Dai, and Y. Han, Enhancing the diffusion of lithium ions to propel sulfur redox for lithium-sulfur batteries. Next Energy, 6100212, 2024. https://doi.org/10.1016/j.nxener.2024.100212

[2] K. Li, M. Liang, H. Wang, X. Wang, Y. Huang, J. Coelho, S. Pinilla, Y. Zhang, F. Qi, V. Nicolosi, and Y. Xu, 3D MXene Architectures for Efficient Energy Storage and Conversion. Adv. Funct. Mater., 30, 2000842, 2020.

[3] J. Nan, X. Guo, J. Xiao, X. Li, W. Chen, W. Wu, H. Liu, Y. Wang, M. Wu, and G. Wang, Nanoengineering of 2D MXene-Based Materials for Energy Storage Application. Small, 17, 1902085, 2021. https://doi.org/10.1002/smll.201902085

[4] .H. Wang and X. Wu, High capacitance of dipicolinic acid-intercalated MXene in neutral water-based electrolyte. Chemical Engineering Journal, 399, 125850, 2020. https://doi.org/10.1016/j.cej.2020.125850

[5] D. Rehnlund, Z. Wang, and L. Nyholm, Lithium-Diffusion Induced Capacity Losses in Lithium-Based Batteries. Adv Mater., 34, 19, 2022. https://doi.org/10.1002/adma.202108827

[6] Y. Guo, H. Wang, X. Feng, Y. Zhao, C. Liang, L. Yang, M. Li, Y. Zhang and W. Gao, 3D MXene microspheres with honeycomb architecture for tumor photothermal/ photodynamic/chemo combination therapy. Nanotechnology, 32, 19, 2021. https://doi.org/10.1088/1361-6528/abe153

[7] X. Chen, Z. Shi, Y. Tian, P. Lin, D. Wu, X. Li, B. Dong, W. Xu and X. Fang, Two-dimensional Ti3C2MXene-based nanostructures for emerging optoelectronic applications. Mater Horizons, 8, 11, 2929–63, 2021. https://doi.org/10.1039/D1MH00986A

[8] H. Xu, A. Ren, J. Wu, and Z. Wang, Recent Advances in 2D MXenes for Photodetection. Adv Funct Mater, 30, 24, 1–16, 2020. https://doi.org/10.1002/adfm.202000907

[9] K. Li, T. H. Chang, Z. Li, H. Yang, F. Fu, and T. Li, Biomimetic MXene Textures with Enhanced Light-to-Heat Conversion for Solar Steam Generation and Wearable Thermal Management. Adv Energy Mater, 9, 34, 1–14, 2019. https://doi.org/10.1002/aenm.201901687

[10] L. Liu, H. Zschiesche, M. Antonietti, M. Gibilaro, P. Chamelot, and L. Massot, In Situ Synthesis of MXene with Tunable Morphology by Electrochemical Etching of MAX Phase Prepared in Molten Salt. Adv Energy Mater, 13, 7, 2023. https://doi.org/10.1002/aenm.202203805

[11] E.A. Hussein, M.M. Zagho, B.R. Rizeq, N.N. Younes, G. Pintus, and K.A. Mahmoud, Plasmonic MXene-based nanocomposites exhibiting photothermal therapeutic effects with lower acute toxicity than pure MXene. Int J Nanomedicine, 14, 4529–39, 2019. https://doi.org/10.2147/IJN.S202208

[12] X. Fan, Y. Ding, Y. Liu, J. Liang, and Y. Chen, Plasmonic Ti3C2Tx MXene Enables Highly Efficient Photothermal Conversion for Healable and Transparent Wearable Device. ACS Nano, 13, 7, 8124–34, 2019. https://doi.org/10.1021/acsnano.9b03161

[13] M.Q. Mehmood, A.R. Shah, M.A. Naveed, N. Mahmood, M. Zubair, and Y. Massoud, MXene-Based Polarization-Insensitive UV-VIS-NIR Meta-Absorber. IEEE Access, 11, 130287–95, 2023. https://doi.org/10.1109/ACCESS.2023.3333533

[14] R. Li, L. Zhang, L. Shi, and P.Wang, MXene Ti3C2: An Effective 2D Light-to-Heat Conversion Material. ACS Nano ,11, 4, 3752–9, 2017. https://doi.org/10.1021/acsnano.6b08415

[15] T.Y. Zhang, H. Wang, J. Tong, J. Zhang, X. Wang, and Y. Zeng, High-efficiency ultraviolet shielding and high transparency of Ti3C2Tx MXene/poly(vinyl alcohol) nanocomposite films. Compos Commun., 33, 101235, 2022. https://doi.org/10.1016/j.coco.2022.101235

[16] B. Xia, X. Zhang, J. Jiang, Y. Wang, T. Li, and Z. Wang, Facile preparation of high strength, lightweight and thermal insulation Polyetherimide/Ti3C2Tx MXenes/Ag nanoparticles composite foams for electromagnetic interference shielding. Compos Commun., 29, 101028, 2022. https://doi.org/10.1016/j.coco.2021.101028

[17] P. Liu, W. Ding, J. Liu, L. Shen, F. Jiang, and P. Liu, Surface termination modification on high-conductivity MXene film for energy conversion. J Alloys Compd, 829, 2020. https://doi.org/10.1016/j.jallcom.2020.154634

[18] M. Naguib, M. Kurtoglu, V. Presser, J. Lu, J. Niu, and M. Heon, Two-dimensional nanocrystals produced by exfoliation of Ti3AlC2. Adv Mater., 23, 37, 4248–53, 2011. https://doi.org/10.1002/adma.201102306

[19] W. Yang, J. J. Byun, J. Yang, F. P. Moissinac, Y. Ma, and H. Ding, All-In-One MXene-Boron Nitride-MXene "oREO" with Vertically Aligned Channels for Flexible Structural Supercapacitor Design. ACS Appl Energy Mater., 4, 8, 7959–72, 2021. https://doi.org/10.1021/acsaem.1c01240

[20] W. Zheng, J. Halim, J. Rosen, and M. W. Barsoum. Aqueous Electrolytes, MXene-Based Supercapacitors and Their Self-Discharge. Adv Energy Sustain Res., 3, 2, 2022. https://doi.org/10.1002/aesr.202100147

[21] K. Hantanasirisakul, M. Q. Zhao, P. Urbankowski, J. Halim, B. Anasori, and S. Kota, Fabrication of Ti3C2Tx MXene Transparent Thin Films with Tunable Optoelectronic Properties. Adv Electron Mater., 2, 6, 1–7, 2016. https://doi.org/10.1002/aelm.201600050

[22] C. Yang, W. Que, X. Yin, Y. Tian, Y. Yang, and M. Que, Improved capacitance of nitrogen-doped delaminated two-dimensional titanium carbide by urea-assisted synthesis. Electrochim Acta., 225, 416–24, 2017. https://dx.doi.org/10.1016/j.electacta.2016.12.173

[23] M. Dahlqvist and J. Rosen. Chalcogen and halogen surface termination coverage in MXenes – structure, stability, and properties. Res Sq.,1–13, 2024. https://www.researchsquare.com/article/rs-4730256/v1?utm_source=researcher_app&utm_medium=referral&utm_campaign=RESR_MRKT_Researcher_inbound

[24] M. Li, J. Lu, K. Luo, Y. Li, K. Chang, and K. Chen, Element Replacement Approach by Reaction with Lewis Acidic Molten Salts to Synthesize Nanolaminated MAX Phases and MXenes. J Am Chem Soc.,141, 11, 4730–7, 2019. https://doi.org/10.1021/jacs.9b00574

[25] F. Alhajri, M. M. Fadlallah, A. Alkhaldi, and A. A. Maarouf, Hybrid MXene-Graphene/Hexagonal Boron Nitride Structures: Electronic and Molecular Adsorption Properties. Nanomaterials,12, 16, 1–13, 2022. https://doi.org/10.3390/nano12162739

[26] B. Miao, T. Bashir, H. Zhang, T. Ali, S. Raza, and D. He, Impact of various 2D MXene surface terminating groups in energy conversion. Renew Sustain Energy Rev.,199, 114506, 2024. https://doi.org/10.1016/j.rser.2024.114506

[27] C. Xu, L. Wang, Z. Liu, L. Chen, J. Guo, and N. Kang, Large-area high-quality 2D ultrathin Mo2C superconducting crystals. Nat Mater.,14, 1135–41, 2015. https://doi.org/10.1038/nmat4374

[28] V. Nesterova, V. Korostelev, and K. Klyukin, Unveiling the Role of Termination Groups in Stabilizing MXenes in Contact with Water. J Phys Chem Lett.,15, 13, 3698–704, 2024. https://doi.org/10.1021/acs.jpclett.4c00045

[29] H. Riazi, S. K. Nemani, M.C. Grady, B. Anasori, and M. Soroush, Ti3C2MXene-polymer nanocomposites and their applications. J Mater Chem A., 9, 8051–98, 2021. https://doi.org/10.1039/D0TA08023C

[30] D. Wang, C. Zhou, A. S. Filatov, W. Cho, F. Lagunas, and S. Vaikuntanathan, Direct synthesis and chemical vapor deposition of 2D carbide and nitride MXenes. Science, 24, 1242-1247, 2023. https://doi.org/10.1126/science.add9204.

[31] Y. Wei, P. Zhang, R. A. Soomro, Q. Zhu, and B. Xu, Advances in the Synthesis of 2D MXenes. Adv Mater., 33, 39, 1–30, 2021. https://doi.org/10.1002/adma.202103148

[32] M. Rahman and M.S. Al Mamun. Future prospects of MXenes: synthesis, functionalization, properties, and application in field effect transistors. Nanoscale Adv., 6, 2, 367–85, 2023. https://doi.org/10.1039/D3NA00874F

[33] X. Li, F. Ran, F. Yang, J. Long, and L. Shao, Advances in MXene Films: Synthesis, Assembly, and Applications, Transactions of Tianjin University. Tianjin University; 27217–247, 2021. https://doi.org/10.1007/s12209-021-00282-y

[34] G. Murali, J.K. Reddy Modigunta, Y.H. Park, J.H. Lee, J. Rawal, and S.Y. Lee, A Review on MXene Synthesis, Stability, and Photocatalytic Applications. ACS Nano,16, 9, 13370–429, 2022. https://doi.org/10.1021/acsnano.2c04750

[35] T. Bashir, S. A. Ismail, J. Wang, W. Zhu, J. Zhao, and L. Gao, MXene terminating groups O, –F or –OH, –F or O, –OH, –F, or O, –OH, –Cl? J Energy Chem.,76, 90–104, 2023. https://doi.org/10.1016/j.jechem.2022.08.032

[36] Y. Zhang, W. Xia, Y. Wu, and P. Zhang, Prediction of MXene based 2D tunable band gap semiconductors: GW quasiparticle calculations. Nanoscale,11, 9, 3993–4000, 2019. https://doi.org/10.1039/C9NR01160A

[37] A. Champagne and J. C. Charlier, Physical properties of 2D MXenes : from a theoretical perspective Journal of Physics, 0–21, 2021. https://doi.org/10.1088/2515-7639/ab97ee

[38] D. Ontiveros, F. Viñes, and C. Sousa, Bandgap engineering of MXene compounds for water splitting. J Mater Chem A., 11,13754–64. 2023. https://doi.org/10.1039/D3TA01933K

[39] J. Lu, I. Persson, H. Lind, J. Palisaitis, M. Li, and Y. Li, Tin+1Cn MXenes with fully saturated and thermally stable Cl terminations. Nanoscale Adv., 9, 3680–5, 2019. https://doi.org/10.1039/C9NA00324J

[40] M. Li, X. Li, G. Qin, K. Luo, J. Lu, and Y. Li, Halogenated Ti3C2 MXenes with Electrochemically Active Terminals for High-Performance Zinc Ion Batteries. ACS Nano, 15, (1), 1077–85, 2021. https://doi.org/10.1021/acsnano.0c07972

[41] L. Liu, E. Raymundo-Piñero, S. Sunny, P. L. Taberna, and P. Simon, Role of Surface Terminations for Charge Storage of Ti3C2Tx MXene Electrodes in Aqueous Acidic Electrolyte. Angew Chemie, 63, 14, 2024. https://doi.org/10.1002/anie.202319238

[42] P. Liu, B. Guan, M. Lu, H. Wang, and Z. Lin, Influence of aqueous solutions treatment on the Li+ storage properties of molten salt derived Ti3C2Clx MXene. Electrochem commun.,136, 107236, 2022. https://doi.org/10.1016/j.elecom.2022.107236

[43] J. Björk and J. Rosen, Functionalizing MXenes by Tailoring Surface Terminations in Different Chemical Environments. Chem Mater.,33, 23, 9108–18, 2021. https://doi.org/10.1021/acs.chemmater.1c01264

[44] J. Chen, Q. Jin, L. Youbing, H. Shao, P. Liu, Y. Liu, P. Taberna, Q. Huang, Z. Lin, and P. Simon, Molten Salt-Shielded Synthesis (MS 3) of MXenes in Air. Energy Environ. Mater., 6, e12328, 2023. https://doi.org/10.1002/eem2.12328

[45] D.D. Kruger, H. García, and A. Primo, Molten Salt Derived MXenes: Synthesis and Applications. Adv Sci., 230, 7106, 2024. https://doi.org/10.1002/advs.202307106

[46] L. Liu, M. Orbay, S. Luo, S. Duluard, H. Shao, and J. Harmel, Exfoliation and Delamination of Ti3C2TxMXene Prepared via Molten Salt Etching Route. ACS Nano, 16, 111–8, 2022. https://doi.org/10.1021/acsnano.1c08498

[47] D. Gandla, Z. Zhuang, V. Jadhav, and D.Q. Tan, Lewis acid molten salt method for 2D MXene synthesis and energy storage applications: A review. Energy Storage Mater., 63, 102977, 2023. https://doi.org/10.1016/j.ensm.2023.102977

[48] T. Zhang, K. Shevchuk, R. Wang, H. Kim, J. Hourani, and Y. Gogotsi, Delamination of Chlorine-Terminated MXene Produced Using Molten Salt Etching. Chem. Mater., 36, 1998−2006, 2024. https://doi.org/10.1021/acs.chemmater.3c02872

[49] X. Liu, Z. Zhang, J. Jiang, C. Tian, X. Wang, and L. Wang, Chlorine-terminated MXene quantum dots for improving crystallinity and moisture stability in high-performance perovskite solar cells. Chem Eng J., 432, 134382, 2022. https://doi.org/10.1016/j.cej.2021.134382

[50] L. Guo, W. Y. Jiang, M. Shen, C. Xu, C. X. Ding, and S. F. Zhao, High capacitance of MXene (Ti3C2Tx) through Intercalation and Surface Modification in Molten Salt. Electrochim Acta, 401, 139476, 2022. https://doi.org/10.1016/j.electacta.2021.139476

[51] K. Arole, J.W. Blivin, S. Saha, D.E. Holta, X. Zhao, and A. Sarmah, Water-dispersible Ti3C2Tz MXene nanosheets by molten salt etching. iScience, 24, 12, 103403, 2021. https://doi.org/10.1016/j.isci.2021.103403

[52] D. Gandla, F. Zhang, and D.Q. Tan, Advantage of Larger Interlayer Spacing of a Mo2Ti2C3 MXene Free-Standing Film Electrode toward an Excellent Performance Supercapacitor in a Binary Ionic Liquid-Organic Electrolyte. ACS Omega, 7, 7190–8, 2022. https://doi.org/10.1021/acsomega.1c06761

[53] Y. Bai, C. Liu, T. Chen, W. Li, S. Zheng, and Y. Pi, MXene-Copper/Cobalt Hybrids via Lewis Acidic Molten Salts Etching for High Performance Symmetric Supercapacitors. Angew Chemie, 60, 48, 25318–22, 2021. https://doi.org/10.1002/anie.202112381

[54] M. Shen, W. Jiang, K. Liang, S. Zhao, R. Tang, and L. Zhang, One-Pot Green Process to Synthesize MXene with Controllable Surface Terminations using Molten Salts. Angew Chemie,133, 52, 27219–24, 2021. https://doi.org/10.1002/anie.202110640

[55] W. Fei, J. Li, L. Ma, T. Zhou, X. Zhu, and X. He, Electrochemically-Switched Microwave Response of MXene in Organic Electrolyte. Adv Mater, 2413311, 1–10, 2024. https://doi.org/10.1002/adma.202413311

[56] J. Nakayama, H. Zhou, J. Izumi, K. Watanabe, K. Suzuki, and F. Nemoto, Electrical Double Layer Formation at Intercalation Cathode–Organic Electrolyte Interfaces During Initial Lithium-Ion Battery Reactions. Adv Mater Interfaces., 11, 5, 1–9, 2024. https://doi.org/10.1002/admi.202300780

[57] C. God, B. Bitschnau, K. Kapper, C. Lenardt, M. Schmuck, and F. Mautner, Intercalation behaviour of magnesium into natural graphite using organic electrolyte systems. RSC Adv., 7, 23, 14168–75, 2017. https://doi.org/10.1039/C6RA28300D

[58] S. Song, F. Yin, Y. Fu, J. Ren, J. Ma, and Y. Liu, Simultaneous regulation of Li-ion intercalation and oxygen termination decoration on Ti3C2Tx MXene toward enhanced oxygen electrocatalysis for Li-O2 batteries. Chem Eng J., 451, 138818, 2023. https://doi.org/10.1016/j.cej.2022.138818

[59] S. Kajiyama, L. Szabova, K. Sodeyama, H. Iinuma, R. Morita, and K. Gotoh, Sodium-Ion Intercalation Mechanism in MXene Nanosheets. ACS Nano,10, 3. 3334–41, 2016. https://doi.org/10.1021/acsnano.5b06958

[60] J. Zhang, L. Xia, L. Yang, J. Li, Y. Liu, and D. Lan, Ti3C2Tx MXene nanobelts with alkali ion intercalation: Dual-purpose for enhanced lithium-ion batteries and microwave absorption. Carbon, 237, 120148, 2025. https://doi.org/10.1016/j.carbon.2025.120148

[61] Y. Wang, J. Li, W. Han, C. Zhao, S. Xu, and D. Wang, Multi-ion competition mechanism within MXene interlayer and Li ion intercalated electrode function. Appl Surf Sci, 623, 157043, 2023. https://doi.org/10.1016/j.apsusc.2023.157043

[62] Y. Yamada, K. Usui, C. H. Chiang, K. Kikuchi, K Furukawa, and A. Yamada, General observation of lithium intercalation into graphite in ethylene-carbonate-free superconcentrated electrolytes. ACS Appl Mater Interfaces, 6, 14, 10892–9, 2014. https://doi.org/10.1021/am5001163

[63] G.J. Wang, Q.T. Qu, B. Wang, Y. Shi, S. Tian, and Y.P. Wu, Electrochemical intercalation of lithium ions into LiV3O8 in an aqueous electrolyte. J Power Sources,189, 1, 503–6, 2009. https://doi.org/10.1016/j.jpowsour.2008.11.006

[64] J. Zhang, Y. Liu, T. Zhao, P. Li, and Y. Sun, Sulfonated Ti3C2Tx to construct proton transfer pathways in polymer electrolyte membrane for enhanced conduction. Solid State Ionics, 310, 100–11, 2017. https://dx.doi.org/10.1016/j.ssi.2017.08.013

[65] X, Li, M. Li, K. Luo, Y. Hou, P. Li, and Q. Yang, Lattice Matching and Halogen Regulation for Synergistically Induced Uniform Zinc Electrodeposition by Halogenated Ti3C2MXenes. ACS Nano,16, 1, 813–22, 2022. https://doi.org/10.1021/acsnano.1c08358

[66] M. Okubo, A. Sugahara, S. Kajiyama, and A. Yamada, MXene as a Charge Storage Host. Acc Chem Res., 51, 3, 591–9, 2018. https://doi.org/10.1021/acs.accounts.7b00481

[67] N. Anju, Noman, Rahman, D. Sen Lazen, and O. I. Okoli, Electrochemical Impedance Analysis of Ti3C2Tx MXene for Pseudocapacitive Charge Storage. J. Compos. Sci., 139, 2025. https://doi.org/10.3390/jcs9030139

[68] K. Paul, A. Khalequea, R. Alia, M. Aly Saad, S. Bacchu, S. Rahman and Z. H. Khan, MXenes from MAX phases: synthesis, hybridization, and advances in supercapacitor applications. RSC Adv., , 15, 8948-8976, 2025. https://doi.org/10.1039/D5RA00271K

[69] S. Mohammadi, S. Ahmadi, H. Navid, R. AzadvaGSanae, M. Fari, Z. Sanae, and M. Moeini, High-capacity freestanding supercapacitor electrode based on electrospun Ti3C2Tx MXene/PANI/PVDF composite. Heliyon, 10, 40482, 2024. https://doi.org/10.1016/j.heliyon.2024.e40482